PHOTONICS Research

Multidimensional trapping by dual-focusing cylindrical vector beams with all-silicon metalens

Jia-Lu Zhu,[1] Ren-Chao Jin,[1] Li-Li Tang,[1] Zheng-Gao Dong,[1,*] Jia-Qi Li,[1,2] and Jin Wang[1]

[1]School of Physics, Southeast University, Nanjing 211189, China
[2]e-mail: lijq@seu.edu.cn
*Corresponding author: zgdong@seu.edu.cn

Received 25 November 2021; revised 3 March 2022; accepted 3 March 2022; posted 7 March 2022 (Doc. ID 449474); published 8 April 2022

Dual-focusing effect with a cylindrical vector-light characteristic (i.e., radial and azimuthal polarizations) is theoretically proposed and numerically demonstrated by spin-decoupled phase control with all-silicon metalens. Attributed to the polarization dependence, the pair of focusing cylindrical vector beams can be interchanged by orthogonally switching the polarization of incident light. We demonstrate the unique contributions of focused radial and azimuthal vector beams to longitudinal and transverse optical forces on glass spheres, respectively, by calculations based on the Maxwell stress tensor. This paper presents the use of all-silicon metalens with highly-compact vector beams, promising for applications such as multidimensional optical trapping. © 2022 Chinese Laser Press

https://doi.org/10.1364/PRJ.449474

1. INTRODUCTION

Cylindrical vector beams (CVBs) with axially symmetric polarizations also called first-order vector beams [1] are generally classified into radially polarized vector beams (RPVBs), azimuthally polarized vector beams (APVBs), and hybridly polarized vector beams [2,3]. On account of the characteristic of inhomogeneous polarization, CVBs can be applied to multifarious fields, such as 3D polarization control [4], optical trapping [5,6], microscopic imaging [7–10], metrology [11–13], and optical communication [14–18]. Moreover, CVBs of the terahertz band, a wave band with plentiful applications of cutting-edge technology [19,20], can also be used for electron acceleration [21] and improve the coupling efficiency of the waveguide [22]. Radially and azimuthally polarized beams as two typical CVBs have been paid more and more attention. RPVBs have significant longitudinally polarized spots when tightly focused [23], making it more efficient for axial optical manipulation of nanoparticles as compared with linearly polarized light [24]. In addition, RPVBs can break the diffraction limit [25], promising for high-resolution lithography and optical sensing [26]. On the other hand, it was demonstrated that APVBs had stronger ability in transverse trapping, in contrast to RPVBs [27–29]. Several technical methods for generating such CVBs were developed, for example, retardation phase plates [23,30,31], subwavelength space-variant metallic gratings [32], and dielectric gratings [33]. Nevertheless, these methods are often plagued by problems, such as bulky size and fabrication difficulty.

Metamaterials as a kind of artificial materials different from natural materials provide an innovative method of optical manipulation [34,35]. Metasurfaces, two-dimensional forms of metamaterials, have also been widely applied in various aspects, such as ultrathin polarizer [36–38], metalens [39,40], and holographic imaging [41,42] for their superior manipulations of amplitude, polarization, and phase on the subwavelength scale. Moreover, emerging all-dielectric metasurfaces can solve the problem of ohmic losses in plasmonic metasurfaces [39,40,43–45]. Therefore, metasurfaces are promising for highly-compact low-loss CVB nanodevices, and, in fact, there have been works on CVB generation [46,47] or focusing [48,49] by metasurfaces. However, there are few works on simultaneously generating RPVBs and APVBs, meanwhile focusing them in multidimensional positions, although recently, the hybrid dual-focusing effect has been demonstrated (i.e., one focusing is a CVB spot, whereas the other is a homogeneously polarized scalar-beam spot). Recently, there have been some works on multifocus metalens, but the vast majority of them concentrated on multifocusing of the phase-vortex beam with a helical wavefront, which is different from our vector beams with inhomogeneous polarization rather than phase [50,51]. In our previous work, we have already experimentally demonstrated multidimensional and multifunctional metalens based on the photonic spin Hall effect [52] as well as spin-dependent dual-wavelength multiplexing metalens [53]. In this paper, we use the design criterion, so-called spin-decoupled phase control previously adopted for the generation of a single CVB [54] to realize multidimensional simultaneous focusing of RPVBs and APVBs based on an all-silicon metalens, indicating that this design criterion is sophisticated for complex vector-light metalenses. Attributed to the anisotropic bar structure, both polarization and wavefront of transmitted light are controlled by the

combined modulation of geometric and dynamic phases. The polarization dependence of the vector beam on incident light determines that the focal positions of both vector beams can be easily exchanged by switching the polarization of incident light, which provides much convenience for practical optical operations. Optical forces of the focused RPVBs and APVBs on a glass sphere were calculated, confirming the contribution of the focusing RPVB (or APVB) to longitudinal (or transverse) optical force. The advantage of this paper for multidimensional simultaneous focusing of RPVBs and APVBs is that multichannel simultaneous manipulation (transverse and longitudinal manipulations) in a multidimensional position can be realized, that is, two kinds of CVBs can be focused or two different types of manipulation (the transverse and longitudinal trappings) can be realized at the same time. Meanwhile, these two kinds of manipulation will not be confined to the same point in space, which is different from a single focused beam of RPVB or APVB that can perform only one manipulation (transverse manipulation or longitudinal manipulation) at a time, and all of these controls will be stuck at the same point in space. In this way, the system of a multidimensional polarization-dependent dual-focusing CVB will enrich the optical control effect [55–57], and more possibilities will be brought to the integration of optical systems.

2. PRINCIPLE

Figure 1(a) shows the elementary bar on a silicon substrate, a simple anisotropic structure usually adopted in literature [36,39,43–45,54]. The silicon bar has a height $h = 200$ μm, parametric lengths a, b, and period $p = 150$ μm. Silicon substrate plays a supporting role and does not affect the polarization distribution of transmitted light. Due to the dielectric characteristic of our metalens design, it is free of ohmic loss on interacting with incident light.

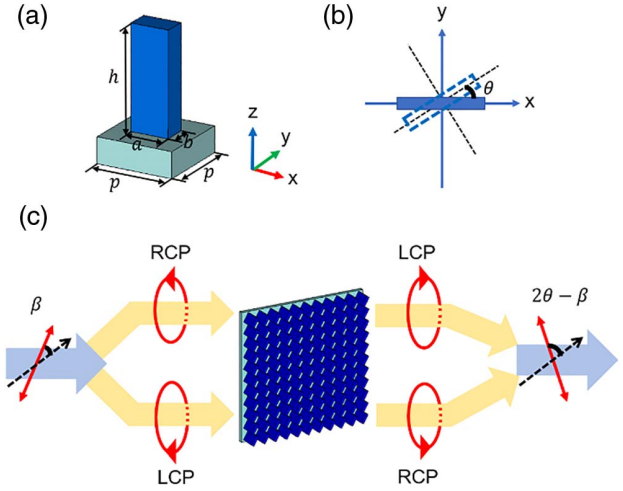

Fig. 1. Schematic of the anisotropic elementary unit and the working principle for the CVB converter. (a) The all-silicon unit configuration consisting of the bar and substrate. (b) The rotation angle θ of the bar is determined by the x axis and the length direction of the bar. (c) The principal diagram of regulating polarization based on the spin-decoupled phase control method where the black dotted lines represent the x axis.

In this paper, we use the spin-decoupled phase control method [54] based on dynamic and geometric phases to generate multidimensional polarization-dependent dual-focusing CVBs. Excitation light is incident normally from the substrate end of the structure. The superposition of the dynamic and geometric phases is used to represent the phase shift due to the interaction between the structure and the incident light,

$$\phi_{\mathrm{LR}} = \varphi_d - 2\theta, \tag{1}$$

$$\phi_{\mathrm{RL}} = \varphi_d + 2\theta. \tag{2}$$

ϕ_{LR} (ϕ_{RL}) represents the phase shift attached to the original incident light where the incident component is right-handed circularly polarized (RCP), left-handed circularly polarized (LCP), and the transmitted component is LCP (RCP). φ_d represents the dynamic phase determined by the size of the bar, and θ is the rotation angle of the bar [Fig. 1(b)]. As shown in Fig. 1(c), the linearly polarized incident light with amplitude E and arbitrary polarization orientation β (the angle with respect to the x axis) is divided into RCP and LCP components with same amplitude of $\frac{E}{2}$ but opposite initial phases of β and $-\beta$, respectively. Upon transmission through the metasurface, RCP and LCP components are converted into cross-polarized LCP and RCP, respectively. As a consequence, these two converted circularly polarized beams may be reconstituted into a linearly polarized beam on the condition that we design the unit cell of the structure to be a perfect half-wave plate. In this ideal circumstance, both circularly polarized components of the incidence are completely converted to orthogonal circular polarizations upon transmission as shown in Fig. 1(c).

For RCP incident component $\left[E_R^{\mathrm{in}} = \frac{E}{2} e^{i\beta} \begin{pmatrix} 1 \\ -i \end{pmatrix}\right]$, it is transmitted to be LCP with

$$E_{\mathrm{LR}} = A \frac{E}{2} e^{i\beta} e^{i\phi_{\mathrm{LR}}} \begin{pmatrix} 1 \\ i \end{pmatrix}, \tag{3}$$

and for the LCP incident component $\left[E_L^{\mathrm{in}} = \frac{E}{2} e^{-i\beta} \begin{pmatrix} 1 \\ i \end{pmatrix}\right]$, it is transmitted to be RCP with

$$E_{\mathrm{RL}} = A \frac{E}{2} e^{-i\beta} e^{i\phi_{\mathrm{RL}}} \begin{pmatrix} 1 \\ -i \end{pmatrix}, \tag{4}$$

where A in Eqs. (3) and (4) represents a constant, ϕ_{LR} and ϕ_{RL} represent the additional phase shifts after the incident light passes through the metasurface. Consequently, the total transmission can be written as

$$
\begin{aligned}
E_t &= E_{\mathrm{LR}} + E_{\mathrm{RL}} = A\frac{E}{2}e^{i\beta}e^{i(\varphi_d-2\theta)}\begin{pmatrix}1\\ i\end{pmatrix} \\
&\quad + A\frac{E}{2}e^{-i\beta}e^{i(\varphi_d+2\theta)}\begin{pmatrix}1\\ -i\end{pmatrix} \\
&= A\frac{E}{2}e^{i\varphi_d}\left[e^{i(\beta-2\theta)}\begin{pmatrix}1\\ i\end{pmatrix} + e^{i(2\theta-\beta)}\begin{pmatrix}1\\ -i\end{pmatrix}\right] \\
&= A\frac{E}{2}e^{i\varphi_d}\begin{pmatrix}e^{i(\beta-2\theta)} + e^{i(2\theta-\beta)}\\ ie^{i(\beta-2\theta)} - ie^{i(2\theta-\beta)}\end{pmatrix} \\
&= 2A\frac{E}{2}e^{i\varphi_d}\begin{pmatrix}\cos(\beta-2\theta)\\ -\sin(\beta-2\theta)\end{pmatrix} \\
&= AEe^{i\varphi_d}\begin{pmatrix}\cos(2\theta-\beta)\\ \sin(2\theta-\beta)\end{pmatrix}. \qquad (5)
\end{aligned}
$$

Equation (5) indicates that the transmitted light is linearly polarized along a direction angle $(2\theta - \beta)$ with respect to the x axis.

In order to achieve a transmission beam with radial polarization $(2\theta_r - \beta = \alpha)$, where $\alpha = a\tan 2(y, x) \in (-\pi, \pi]$ is the polar angle, and θ_r represents the rotation angle of the bar. Then, for this RPVB case, we get

$$\theta_r = \frac{\alpha + \beta}{2}. \qquad (6)$$

To achieve azimuthally polarized transmission, i.e., $2\theta_a - \beta = \alpha - 90°$, θ_a represents the rotation angle of the bar for the APVB case, which, thus, satisfies

$$\theta_a = \frac{\alpha - 90° + \beta}{2}. \qquad (7)$$

It is noted that for the respective bar with determined rotation direction θ_r (or θ_a), changing the incident polarization angle β in Fig. 1(c) to its orthogonal direction, the transmitted light will be switched from a radially (or azimuthally) polarized to an azimuthally (or radially) polarized CVB.

In addition, as the dynamic phase, φ_d in Eq. (5) plays the role of controlling the phase wavefront of transmitted light. In order to realize highly-compact focusing CVB, φ_d needs to meet the following equation:

$$\varphi_d = \frac{360°}{\lambda}\left[\sqrt{(x - x_1)^2 + (y - y_1)^2 + f^2} - f\right], \qquad (8)$$

where λ represents the wavelength of incident light and f represents the focal length, that is, the distance between the metasurface and the focal point (x_1, y_1, f). According to the above design method, we can realize multidimensional polarization-dependent dual-focusing CVB.

3. RESULTS AND DISCUSSION

A. Design of Elementary Unit

Before assembling metalens with the corresponding properties, elementary bars with suitable sizes are optimized not only to satisfy the half-wave plate condition (phase difference π and equal amplitude for the orthogonal polarization components of transmission) for CVB polarization modulation, but also to satisfy the evolution of the dynamic phase in the range of 0–2π for CVB focusing. As shown in Fig. 2, the database of transmission amplitude and phase shift (t_{xx}, t_{yy}, φ_{xx}, φ_{yy}) in dependence of bar size (a and b) at 1-THz incidence is established, where t_{xx} (t_{yy}) and φ_{xx} (φ_{yy}) represent the transmission amplitude and the additional phase shift of transmitted x-polarized (y-polarized) light at the incidence of x-polarized (y-polarized) light, respectively. By choosing bar sizes to meet $t_{yy} = t_{xx}$ and $|\varphi_{yy} - \varphi_{xx}| = \pi$, we pick eight bars out with dimensions of $a = 87.35$, 49.6, 49.52, 45.31, 30.9, 103.8, 79.45, 74.74 μm and, correspondingly, $b = 30.9$, 103.8, 79.45, 74.74, 87.35, 49.6, 49.52, 45.31 μm.

In order to verify whether these eight bars meet the conditions of half-wave plates and explore the working bandwidth of the bars, amplitudes (t_{xx}, t_{yy}) and phase shifts (φ_{xx}, φ_{yy}) together with their respective differences as a function of the incident frequency are shown in Figs. 3(a)–3(f). When the incident frequency is 1 THz, obviously, for each of the eight bars, the difference between phase shifts of transmission is always about π. Meanwhile, the amplitude difference between t_{xx}

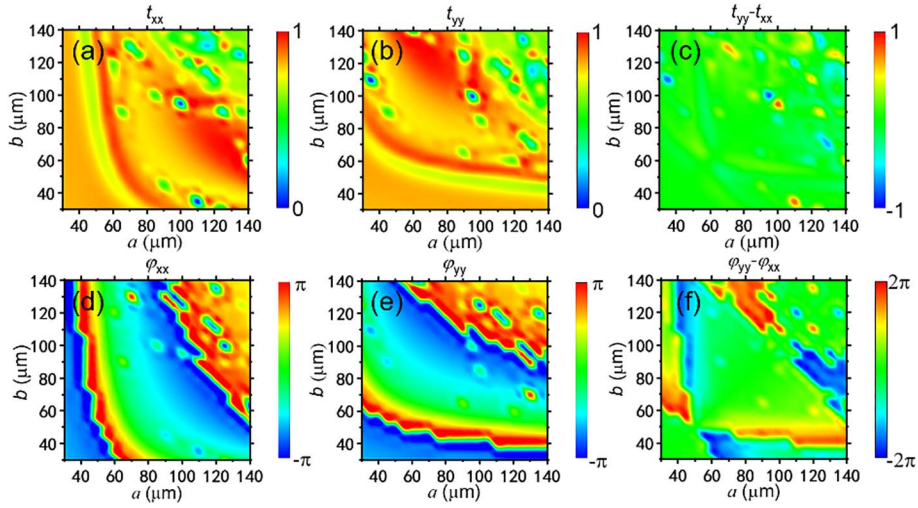

Fig. 2. Simulation of transmission amplitude (t_{xx}, t_{yy}), phase shift (φ_{xx}, φ_{yy}), and respective differences in the dependence of the bar sizes (a, b) at 1-THz incidence.

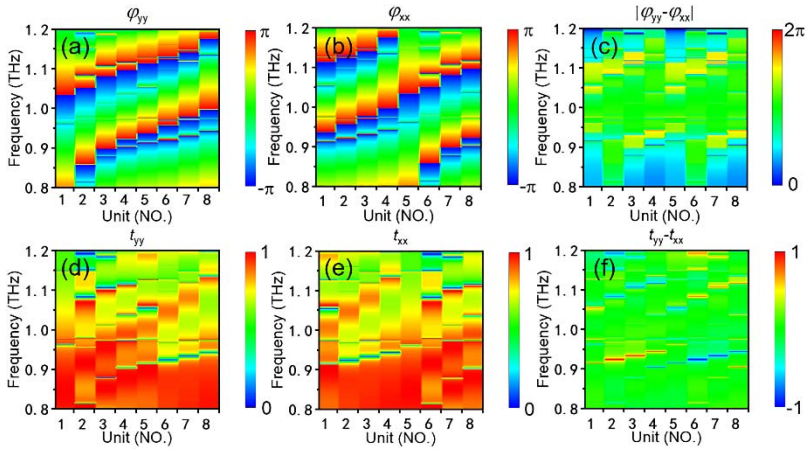

Fig. 3. Simulated amplitude (t_{xx}, t_{yy}), amplitude difference ($t_{yy} - t_{xx}$), phase shift (φ_{xx}, φ_{yy}), and phase-shift difference $|\varphi_{yy} - \varphi_{xx}|$ as a function of the incident frequency, which confirms the property of the half-wave plate and the 2π dynamic phase coverage of 1–8 bars.

and t_{yy} remains around zero. In addition, it can be found from Fig. 3(b) that at 1 THz, the dynamic phases $\varphi_d = \varphi_{xx}$ do satisfy a gradient variation with a step of $\frac{\pi}{4}$ and cover the full 2π-modulation preference. Unfortunately, these bars cannot maintain superior half-wave plate characteristics over a wide spectral range, that is, the working bandwidth is only about 0.1 THz.

Next, with the amplitude and phase databases for eight bars, we design the arrangement of elements based on the aforesaid design principle, which is feasible to realize multidimensional dual-focusing CVB.

B. Transverse Dual-Focusing Terahertz Vector Beams

Figure 4 illustrates the schematic of a transverse dual-focusing CVB system. For simplicity, the incident light is assumed to be x polarized, which is split into double CVB focal points at the coordinates of $(x_1, 0, f)$ and $(x_2, 0, f)$. The former one is APVB, whereas the latter is RPVB, and we set $x_1 = -500$ μm, $x_2 = 500$ μm, and focal length $f = 1200$ μm. The enlarged view of the metalens (Fig. 4 inset) is divided into blue and pink regions, corresponding to focal spots with azimuthal and radial polarizations at x_1 and x_2, respectively. The rotation angles of the bar and dynamic phase in these two regions are θ_a and φ_{d1} for the APVB spot at x_1 (or θ_r and φ_{d2} for the RPVB at x_2), which satisfy Equations (6)–(8), respectively.

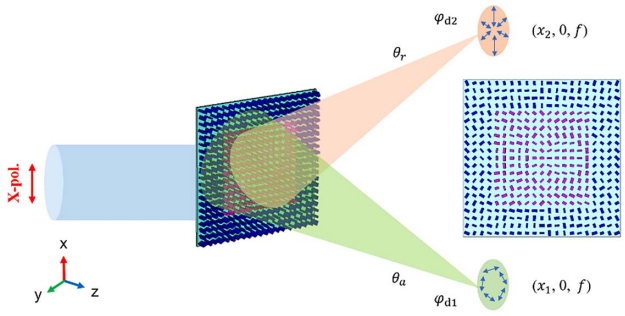

Fig. 4. Schematic of the transverse dual-focusing CVB system. The inset on the right illustrates the specific arrangement of metasurface elements.

Figure 5 shows the finite-difference time-domain simulation results of the transverse dual-focusing CVB system. It can be clearly found from Fig. 5(a) that there are two CVB focal spots separated perpendicular to the propagation direction of incident light, namely, the transverse x direction where polarization distributions are azimuthally polarized (focus x_1) and radially polarized (focus x_2), respectively. In order to make the polarization distribution at the focal points clearer, Fig. 5(a) has been appropriately enlarged compared with Figs. 5(c)–5(f). The radial polarization distribution at focus x_2 is slightly distorted because there is, in fact, an angle γ between the intercepted x–y plane [black dashed line in Fig. 5(b)] and the section where the true radial polarization is located [pink solid line in Fig. 5(b)], and the polarization distribution at focus x_1 can also be understood in this way. Figure 5(b) shows the E-field intensity distribution on the x–z plane with $y = 0$ μm. Figures 5(c)–5(f) present the E-field intensity map on the x–y plane with $z = 1200$ μm. The doughnut shape in Fig. 5(c) confirms the focusing characteristic of APVB. Figures 5(d) and 5(e) illustrate that, for the APVB focusing at x_1, $|E_x|^2$ (or $|E_y|^2$) is mainly distributed along the y (or x) direction, i.e., perpendicular to the polarization direction, verifying the focus at x_1 is azimuthally polarized. Inversely, the $|E_x|^2$ (or $|E_y|^2$) component for focus x_2 is mainly distributed along the x (or y) direction, i.e., parallel to the polarization direction, indicating the radially polarized characteristic of focus x_2. Thus, the transverse dual-focusing CVB effect is achieved. The phenomenon that the longitudinal component of the focal spot of radially polarized light [Fig. 5(f)] does not dominate the intensity distribution of the focal spot [Fig. 5(c)] as expected is due to the fact that the radially polarized beam is not focused tightly enough [1,23].

C. Longitudinal Dual-Focusing Terahertz Vector Beams

The longitudinal dual-focusing CVB system is illustrated in Fig. 6. Similarly, x-polarized light is incident normally onto the silicon substrate, it transmits through the two regions

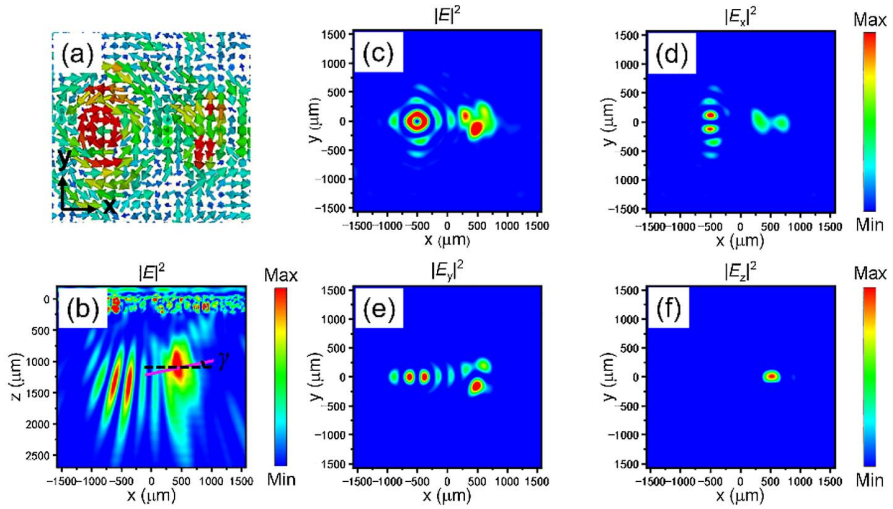

Fig. 5. Simulation results of the transverse dual-focusing CVB system under the incidence of x-polarized light. (a) The distribution of E-field vectors on the x–y plane with $z = 1200$ μm. (b) Total E-field intensity distribution on the x–z plane with $y = 0$ μm. (c)–(f) E-field maps on the x–y plane with $z = 1200$ μm. The black dashed line and the pink solid line in (b) indicate the x–y plane with $z = 1200$ μm and the plane where the true radial polarizations are located, respectively.

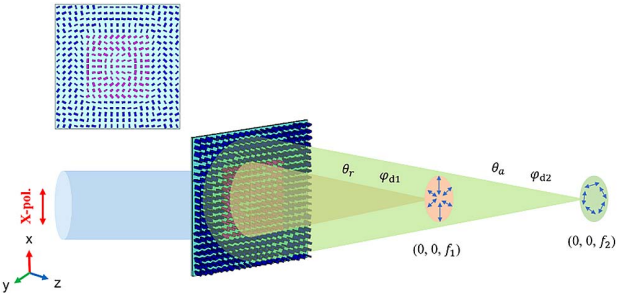

Fig. 6. Schematic of the longitudinal dual-focusing CVB system. The top inset illustrates the arrangement of the bar elements.

(pink and blue) of the metalens, and then longitudinally generates two CVB focusing spots with radial and azimuthal polarizations at positions $(0, 0, f_1)$ and $(0, 0, f_2)$, respectively, where we set $f_1 = 1200$ μm and $f_2 = 3300$ μm. The focal lengths of the system have been predetermined in the theoretical design of the structure. As long as the incident condition (i.e., the incident light frequency is 1 THz, and the incident light is normally incident from the substrate end of structure) is satisfied in the experiment, the desired focal spots will be generated at specific focal positions. Therefore, no additional manipulation is required to control the focal lengths experimentally.

Figures 7(a) and 7(b) illustrate the E-field distribution of the longitudinal dual-focusing CVB system, verifying the radial and azimuthal distributions, respectively. Figures 7(c)–7(e) illustrate the E-field intensity map on the x–z plane with $y = 0$ μm. In Fig. 7(c), two focusing spots are separately generated at $z = 1200$ and 3300 μm. The $|E_y|^2$ map on the x–z plane in Fig. 7(d) indicates the APVB characteristic for the focal spot at $z = 3300$ μm, whereas, the $|E_z|^2$ map in Fig. 7(e) shows the RPVB tight-focusing characteristic at $z = 1200$ μm.

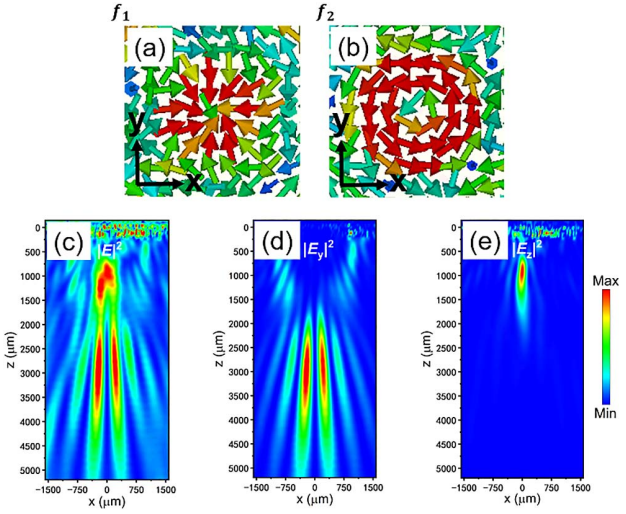

Fig. 7. Simulation results of the longitudinal dual-focusing CVB system under the incidence of x-polarized light. (a) and (b) Distributions of E-field vectors on the x–y plane with $z = 1200$ μm (focus f_1) and 3300 μm (focus f_2), respectively. (c)–(e) E-field maps on the x–z plane with $y = 0$ μm.

1. Polarization Dependence

As can be found from the principle described in Section 2, the polarization distribution at the focal position can be switched from radial/azimuthal polarization to azimuthal/radial polarization by converting the polarization direction of the incident light orthogonally. Taking the longitudinal dual-focusing metalens as an example, converting the incident light from x to y polarization will lead to an exchange between the azimuthally and the radially polarized focal spots.

Figures 8(a) and 8(b) show simulation results to confirm the polarization dependence of our longitudinal dual-focusing

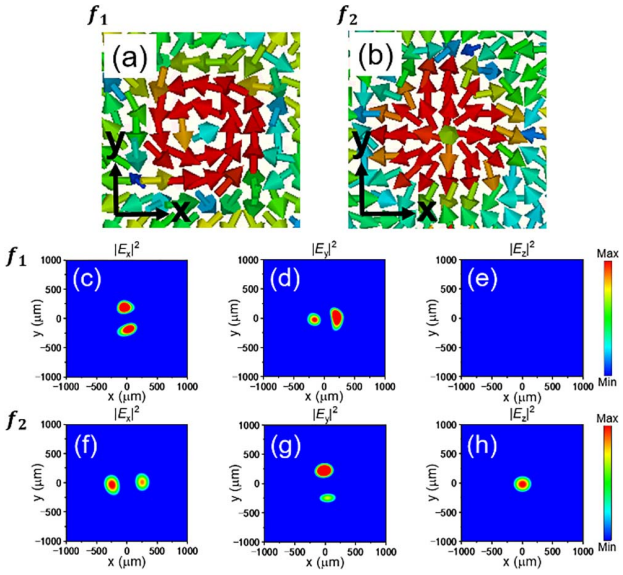

Fig. 8. Simulation results of the longitudinal polarization-dependent dual-focusing CVB system under the incidence of y-polarized light. (a) and (b) E-field distributions on the x–y plane with $z = 1200$ μm (focus f_1) and 3300 μm (focus f_2). (c)–(h) E-field intensity maps on the f_1 and f_2 focal planes.

CVB metalens. Obviously, the original focal spot with radial/azimuthal polarization does interconvert into a focal spot with orthogonal azimuthal/radial polarization. Figures 8(c)–8(h) can verify the azimuthal and radial polarization characteristics at spots f_1 and f_2, respectively, as discussed earlier.

2. Calculation of Optical Force

Taking the longitudinal dual-focusing CVB system as an example, based on the ray tracing method [24,27,58], optical forces, corresponding to the tight-focusing fields of APVB and RPVB, were calculated to investigate the characteristics of tiny particle manipulation by such dual-focusing CVBs, which should contribute to multidimensional vector-light tweezers.

For simplicity, we consider the optical forces stressed by the focused RPVB (or APVB) at focal point f_1 in the longitudinal dual-focusing system under the x- (or y-) polarized incidence. A glass sphere with refractive index of 1.56 and radius of 300 μm was used as the stressed object as shown in Fig. 9(a).

Figure 9(b) illustrates the calculated longitudinal optical force F_z of RPVB focusing at f_1 under x-polarized incident light. Figures 9(c) and 9(d) illustrate the calculated transverse optical forces F_x and F_y of APVB focusing at f_1 under y-polarized incident light. The insets illustrate the planar E-field distributions, where Δz and Δx (or Δy) represent the displacement between the sphere center and the focal point f_1 along the longitudinal and transverse directions, respectively. It can be clearly found that the focused RPVB and APVB contribute to the longitudinal and transverse trapping characteristics on the glass sphere, respectively. Taking Fig. 9(c) as an example, when the sphere is deviated from the focal point ($\Delta x \neq 0$), F_x shows nonzero values. Depending on the offset in different directions, the forces are always toward the focus.

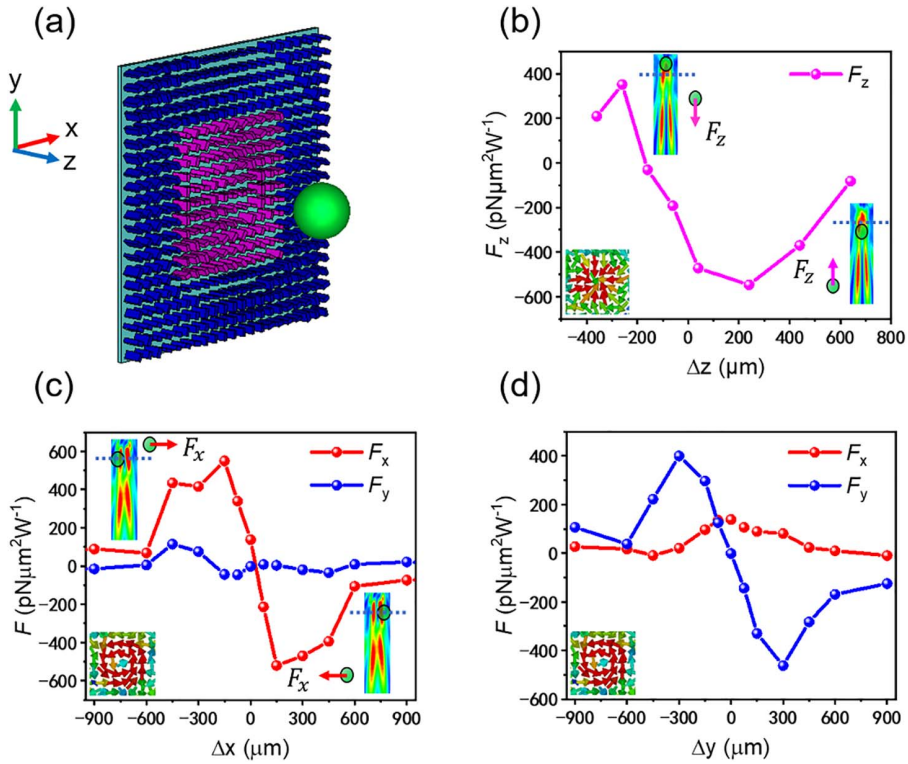

Fig. 9. Calculation results of the optical force. (a) Schematic of the longitudinal dual-focusing CVB metalens and the glass sphere which is subjected to the optical force. (b) Calculated longitudinal optical force F_z of the RPVB focusing at f_1 under x-polarized incident light. (c) and (d) Calculated transverse optical forces F_x and F_y of the APVB focusing at f_1 under y-polarized incident light. The dashed lines in (b) and (c) indicate the focal plane. The insets in the lower left corners in (b)–(d) show E-field distributions at corresponding focal planes.

That is, the sphere will always be subjected to a force pulling it back to the equilibrium position until it finally stabilizes there, so-called optical trapping. The absorption of glass spheres may have a certain influence on the simulation results, but it will not affect the trend of the optical force, which acts as the trapping force. What needs to be paid attention to is that for the small longitudinal component as discussed in Fig. 5(f) in Section 3.B, the longitudinal gradient force F_z that we calculated in Fig. 9(b) may not be able to overcome the gravity force of the glass sphere and trap the glass sphere longitudinally in the experiment, which has nothing to do with the size of the glass sphere because both optical and gravitational forces are dependent on the particle radius as r^3 (r represents the radius of the glass sphere). Therefore, further research and improvement are still needed to experimentally realize longitudinal trapping. Nevertheless, such a tiny trapping force is still meaningful for situations, such as bonding rather than levitation. Moreover, the trapping effect is not limited to the considered silica particle, and it is, in principle, also applicable for other absorptive objects enduring the focusing vector fields. It is worth discussing the special case that the incident light is neither x polarized nor y polarized; instead, the incident light is the superposition of x-polarized incidence and y-polarized incidence in which the transmitted light will exert both longitudinal and transverse optical forces on the glass sphere at the same time if the interference of optical forces can be ignored.

4. CONCLUSION

In this paper, the multidimensional dual-focusing CVB metalens with an all-silicon configuration was proposed under the design principle of spin-decoupled phase control from which a pair of focused vector beams with radial and azimuthal polarizations can be generated in the transverse as well as the longitudinal directions. Furthermore, we calculated the optical forces of such APVB and RPVB focusing spots exerted on a glass sphere and, consequently, revealed the transverse and longitudinal trapping characteristics, attributed to the hollow singularity of APVB and to the convergence singularity of RPVB in the case of focusing, respectively. Moreover, the polarization distributions of the dual-focusing CVB metalens can be interchanged by simply switching the polarization direction of incident light, providing much convenience in multidimensional multichannel optical trapping by focused vector beams. What needs to be pointed out is that our paper only considered forces of APVB and RPVB acting on the glass sphere and numerically proved the transverse and longitudinal trapping forces of these two focused vector beams on the glass sphere. Further research is needed to trap the sphere experimentally. For example, for the focused RPVB in this paper, its longitudinal trapping force is not large enough to fight against other forces, if any, such as the gravity force of the glass sphere or air resistance, and considering the difficulty of providing incident power strong enough in the experiment if we really want to experimentally achieve the longitudinal trapping of the sphere against its gravity with the focused RPVB, Some effort, such as adjusting the operating band to the visible/near-infrared band is necessary to improve the trapping force. Lastly, it is noted that the design strategy, so-called spin-decoupled phase control, can be extended to high-order vector beams, promising for the high integration of the optical system with potential applications in polarization-dependent optical communication, information encryption, imaging, and so on.

Funding. National Natural Science Foundation of China (11774053, 12174052); Open Project from Key Laboratory of MEMS of the Ministry of Education; Fundamental Research Funds for the Central Universities (2242021k30012).

Disclosures. The authors declare no conflicts of interest.

Data Availability. The data that support the findings of this paper are available within the paper.

REFERENCES

1. E. Otte and C. Denz, "Optical trapping gets structure: structured light for advanced optical manipulation," Appl. Phys. Rev. **7**, 041308 (2020).
2. J. Li, S. Chen, H. Yang, J. Li, P. Yu, H. Cheng, C. Gu, H.-T. Chen, and J. Tian, "Simultaneous control of light polarization and phase distributions using plasmonic metasurfaces," Adv. Funct. Mater. **25**, 704–710 (2015).
3. Q. W. Zhan, "Cylindrical vector beams: from mathematical concepts to applications," Adv. Opt. Photon. **1**, 1–57 (2009).
4. X. Li, T. H. Lan, C. H. Tien, and M. Gu, "Three-dimensional orientation-unlimited polarization encryption by a single optically configured vectorial beam," Nat. Commun. **3**, 998 (2012).
5. N. Bhebhe, C. Rosales-Guzmán, and A. Forbes, "Classical and quantum analysis of propagation invariant vector flat-top beams," Appl. Opt. **57**, 5451–5458 (2018).
6. Y. Zhao, Q. Zhan, Y. Zhang, and Y.-P. Li, "Creation of a three-dimensional optical chain for controllable particle delivery," Opt. Lett. **30**, 848–850 (2005).
7. R. Chen, K. Agarwal, C. J. R. Sheppard, and X. D. Chen, "Imaging using cylindrical vector beams in a high-numerical-aperture microscopy system," Opt. Lett. **38**, 3111–3114 (2013).
8. M. Yoshid, Y. Kozawa, and S. Sato, "Subtraction imaging by the combination of higher-order vector beams for enhanced spatial resolution," Opt. Lett. **44**, 883–886 (2019).
9. S. Segawa, Y. Kozawa, and S. Sato, "Resolution enhancement of confocal microscopy by subtraction method with vector beams," Opt. Lett. **39**, 3118–3121 (2014).
10. S. Segawa, Y. Kozawa, and S. Sato, "Demonstration of subtraction imaging in confocal microscopy with vector beams," Opt. Lett. **39**, 4529–4532 (2014).
11. F. Töppel, A. Aiello, C. Marquardt, E. Giacobino, and G. Leuchs, "Classical entanglement in polarization metrology," New J. Phys. **16**, 073019 (2014).
12. S. Berg-Johansen, F. Töppel, B. Stiller, P. Banzer, M. Ornigotti, E. Giacobino, G. Leuchs, A. Aiello, and C. Marquardt, "Classically entangled optical beams for high-speed kinematic sensing," Optica **2**, 864–868 (2015).
13. M. Neugebauer, P. Wozniak, A. Bag, G. Leuchs, and P. Banzer, "Polarization-controlled directional scattering for nanoscopic position sensing," Nat. Commun. **7**, 11286 (2016).
14. B. Ndagano, I. Nape, M. A. Cox, C. Rosales-Guzmán, and A. Forbes, "Creation and detection of vector vortex modes for classical and quantum communication," J. Lightwave Technol. **36**, 292–301 (2018).
15. G. Milione, T. A. Nguyen, J. Leach, D. A. Nolan, and R. R. Alfano, "Using the nonseparability of vector beams to encode information for optical communication," Opt. Lett. **40**, 4887–4890 (2015).
16. V. D'Ambrosio, G. Carvacho, F. Graffitti, C. Vitelli, B. Piccirillo, L. Marrucci, and F. Sciarrino, "Entangled vector vortex beams," Phys. Rev. A **94**, 030304 (2016).

17. J. Liu, S. M. Li, L. Zhu, A. D. Wang, S. Chen, C. Klitis, C. Du, Q. Mo, M. Sorel, S. Y. Yu, X. L. Cai, and J. Wang, "Direct fiber vector eigenmode multiplexing transmission seeded by integrated optical vortex emitters," Light Sci. Appl. **7**, 17148 (2018).
18. D. Chen, S.-H. Zhao, L. Shi, and Y. Liu, "Measurement-device-independent quantum key distribution with pairs of vector vortex beams," Phys. Rev. A **93**, 032320 (2016).
19. M. Tonouchi, "Cutting-edge terahertz technology," Nat. Photonics **1**, 97–105 (2007).
20. W. He, M. Tong, Z. Xu, Y. Hu, X. A. Cheng, and T. Jiang, "Ultrafast all-optical terahertz modulation based on an inverse-designed metasurface," Photon. Res. **9**, 1099–1108 (2021).
21. E. A. Nanni, W. R. Huang, K.-H. Hong, K. Ravi, A. Fallahi, G. Moriena, R. D. Miller, and F. X. Kärtner, "Terahertz-driven linear electron acceleration," Nat. Commun. **6**, 8486 (2015).
22. J. A. Deibel, K. Wang, M. D. Escarra, and D. M. Mittleman, "Enhanced coupling of terahertz radiation to cylindrical wire waveguides," Opt. Express **14**, 279–290 (2006).
23. S. Quabis, R. Dorn, M. Eberler, O. Glöckl, and G. Leuchs, "Focusing light to a tighter spot," Opt. Commun. **179**, 1–7 (2000).
24. M. Michihata, T. Hayashi, and Y. Takaya, "Measurement of axial and transverse trapping stiffness of optical tweezers in air using a radially polarized beam," Appl. Opt. **48**, 6143–6151 (2009).
25. R. Zuo, W. Liu, H. Cheng, S. Chen, and J. Tian, "Breaking the diffraction limit with radially polarized light based on dielectric metalenses," Adv. Opt. Mater. **6**, 1800795 (2018).
26. F. Yue, D. Wen, J. Xin, B. D. Gerardot, J. Li, and X. Chen, "Vector vortex beam generation with a single plasmonic metasurface," ACS Photon. **3**, 1558–1563 (2016).
27. Y. Kozawa and S. Sato, "Optical trapping of micrometer-sized dielectric particles by cylindrical vector beams," Opt. Express **18**, 10828–10833 (2010).
28. S. E. Skelton, M. Sergides, R. Saija, M. A. Iatì, O. M. Maragó, and P. H. Jones, "Trapping volume control in optical tweezers using cylindrical vector beams," Opt. Lett. **38**, 28–30 (2013).
29. M. G. Donato, S. Vasi, R. Sayed, P. H. Jones, F. Bonaccorso, A. C. Ferrari, P. G. Gucciardi, and O. M. Maragó, "Optical trapping of nanotubes with cylindrical vector beams," Opt. Lett. **37**, 3381–3383 (2012).
30. S. Quabis, R. Dorn, and G. Leuchs, "Generation of a radially polarized doughnut mode of high quality," Appl. Phys. B **81**, 597–600 (2005).
31. G. Machavariani, Y. Lumer, I. Moshe, A. Meir, and S. Jackel, "Efficient extracavity generation of radially and azimuthally polarized beams," Opt. Lett. **32**, 1468–1470 (2007).
32. Z. Bomzon, V. Kleiner, and E. Hasman, "Pancharatnam–Berry phase in space-variant polarization-state manipulations with subwavelength gratings," Opt. Lett. **26**, 1424–1426 (2001).
33. Z. Bomzon, G. Biener, V. Kleiner, and E. Hasman, "Radially and azimuthally polarized beams generated by space-variant dielectric subwavelength gratings," Opt. Lett. **27**, 285–287 (2002).
34. Y. Liu and X. Zhang, "Metamaterials: a new frontier of science and technology," Chem. Soc. Rev. **40**, 2494–2507 (2011).
35. D. Lee, S. So, G. Hu, M. Kim, T. Badloe, H. Cho, J. Kim, H. Kim, C. Qiu, and J. Rho, "Hyperbolic metamaterials: fusing artificial structures to natural 2D materials," eLight **2**, 1 (2022).
36. Z. C. Liu, Z. C. Li, Z. Liu, H. Cheng, W. W. Liu, C. C. Tang, C. Z. Gu, J. J. Li, H. T. Chen, S. Q. Chen, and J. G. Tian, "Single-layer plasmonic metasurface half-wave plates with wavelength-independent polarization conversion angle," ACS Photon. **4**, 2061–2069 (2017).
37. B. Bai, Y. Svirko, J. Turunen, and T. Vallius, "Optical activity in planar chiral metamaterials: theoretical study," Phys. Rev. A **76**, 023811 (2007).
38. A. Drezet, C. Genet, J.-Y. Laluet, and T. W. Ebbesen, "Optical chirality without optical activity: how surface plasmons give a twist to light," Opt. Express **16**, 12559–12570 (2008).
39. M. Khorasaninejad, W. T. Chen, R. C. Devlin, J. Oh, A. Y. Zhu, and F. Capasso, "Metalenses at visible wavelengths: diffraction-limited focusing and subwavelength resolution imaging," Science **352**, 1190–1194 (2016).
40. E. Arbabi, A. Arbabi, S. M. Kamali, Y. Horie, and A. Faraon, "Multiwavelength polarization-insensitive lenses based on dielectric metasurfaces with meta-molecules," Optica **3**, 628–633 (2016).
41. G. Zheng, H. Muehlenbernd, M. Kenney, G. Li, T. Zentgraf, and S. Zhang, "Metasurface holograms reaching 80% efficiency," Nat. Nanotechnol. **10**, 308–312 (2015).
42. J. P. B. Mueller, N. A. Rubin, R. C. Devlin, B. Groever, and F. Capasso, "Metasurface polarization optics: independent phase control of arbitrary orthogonal states of polarization," Phys. Rev. Lett. **118**, 113901 (2017).
43. T. Li, X. Xu, B. Fu, S. Wang, B. Li, Z. Wang, and S. Zhu, "Integrating the optical tweezers and spanner onto an individual single-layer metasurface," Photon. Res. **9**, 1062–1068 (2021).
44. S. Gao, C. S. Park, S. S. Lee, and D. Y. Choi, "All-dielectric metasurface for simultaneously realizing polarization rotation and wavefront shaping for visible light," Nanoscale **11**, 4083–4090 (2019).
45. Y. Hu, X. Wang, X. Luo, X. Ou, L. Li, Y. Chen, Y. Ping, S. Wang, and H. Duan, "All-dielectric metasurfaces for polarization manipulation: principles and emerging applications," Nanophotonics **9**, 3755–3780 (2020).
46. D. Wang, T. Liu, Y. Zhou, X. Zheng, S. Sun, Q. He, and L. Zhou, "High-efficiency metadevices for bifunctional generations of vectorial optical fields," Nanophotonics **10**, 685–695 (2020).
47. W. Shu, Y. Liu, Y. Ke, X. Ling, Z. Liu, B. Huang, H. Luo, and X. Yin, "Propagation model for vector beams generated by metasurfaces," Opt. Express **24**, 21177–21189 (2016).
48. Y. Liu, Y. Ke, J. Zhou, Y. Liu, H. Luo, S. Wen, and D. Fan, "Generation of perfect vortex and vector beams based on Pancharatnam-Berry phase elements," Sci. Rep. **7**, 44096 (2017).
49. F. Zhang, H. Yu, J. Fang, M. Zhang, S. Chen, J. Wang, A. He, and J. Chen, "Efficient generation and tight focusing of radially polarized beam from linearly polarized beam with all-dielectric metasurface," Opt. Express **24**, 6656–6664 (2016).
50. C. Zheng, J. Li, G. Wang, S. Wang, J. Li, H. Zhao, H. Zang, Y. Zhang, Y. Zhang, and J. Yao, "Fine manipulation of terahertz waves via all-silicon metasurfaces with an independent amplitude and phase," Nanoscale **13**, 5809–5816 (2021).
51. S. Gao, C. Park, C. Zhou, S. Lee, and D. Choi, "Twofold polarization-selective all-dielectric trifoci metalens for linearly polarized visible light," Adv. Opt. Mater. **7**, 1900883 (2019).
52. R. Jin, L. Tang, J. Li, J. Wang, Q. Wang, Y. Liu, and Z.-G. Dong, "Experimental demonstration of multidimensional and multifunctional metalenses based on photonic spin Hall effect," ACS Photon. **7**, 512–518 (2020).
53. L. Tang, R. Jin, Y. Cao, J. Li, J. Wang, and Z. G. Dong, "Spin-dependent dual-wavelength multiplexing metalens," Opt. Lett. **45**, 5258–5261 (2020).
54. Y. Xu, H. Zhang, Q. Li, X. Zhang, Q. Xu, W. Zhang, C. Hu, X. Zhang, J. Han, and W. Zhang, "Generation of terahertz vector beams using dielectric metasurfaces via spin-decoupled phase control," Nanophotonics **9**, 3393–3402 (2020).
55. I. D. Stoev, B. Seelbinder, E. Erben, N. Maghelli, and M. Kreysing, "Highly sensitive force measurements in an optically generated, harmonic hydrodynamic trap," eLight **1**, 7 (2021).
56. H. Li, Y. Y. Cao, L. M. Zhou, X. H. Xu, T. T. Zhu, Y. Z. Shi, C. W. Qiu, and W. Q. Ding, "Optical pulling forces and their applications," Adv. Opt. Photon. **12**, 288–366 (2020).
57. D. Gao, W. Ding, M. Nieto-Vesperinas, X. Ding, M. Rahman, T. Zhang, C. Lim, and C. W. Qiu, "Optical manipulation from the microscale to the nanoscale: fundamentals, advances and prospects," Light Sci. Appl. **6**, e17039 (2017).
58. T. A. Nieminen, N. R. Heckenberg, and H. Rubinsztein-Dunlop, "Forces in optical tweezers with radially and azimuthally polarized trapping beams," Opt. Lett. **33**, 122–124 (2008).